

1 **Author Response to Interactive comment on “Reflection tomography of time-lapse GPR data for studying dynamic**
2 **unsaturated flow phenomena” by Adam R. Mangel et al.**

3 This response is directed toward the comments left by Anonymous Referee #1, posted to the Hydrology and Earth
4 Systems Sciences (HESS) discussion board for manuscript [hess-2018-230](#) on August 5, 2018.

5 First and foremost, the authors would like to thank Anonymous Referee #1 (AR1) for devoting time to reviewing our
6 manuscript and for providing a critical review of the content. Below, the authors have outlined responses to individual
7 comments made by the reviewer.

8 *ARI: Yet, I have found it to a large extent disappointing that the authors seem to give too much credit to their own*
9 *past work, and neglect a large body of literature considering multi-offset GPR processing, that dates back at least a*
10 *couple of decades.*

11 **Author Response:** The authors have added additional references for processing of multi-offset GPR data as suggested
12 by the reviewer.

13 *ARI: Even more serious, is the lack of proper reference to wave migration methods that are state of the art in*
14 *industrial seismic processing, and are yet presented herewith as if they are novel, or at least rediscovered by the*
15 *authors.*

16 **Author Response:** The authors have added additional references for wave migration methods as suggested by the
17 reviewer. The authors do not claim to have ‘rediscovered’ the methods used but are simply the first to apply them to
18 time-lapse GPR data for imaging dynamic hydrologic conditions, which is novel.

19 *ARI: From a technical viewpoint, I am a bit puzzled by the error estimates for water content estimates that is 5-10%*
20 *in vol/vol (is it saturation or moisture content?) – as compared to 5-15% from soil moisture probes (again, same*
21 *question). I feel this error is too high to make the estimates useful (if it is moisture content as I read it!). Note that in*
22 *cross-hole GPR usually 2-3% error in volumetric moisture content is generally accepted as realistic.*

23 **Author Response:** All soil moisture data is reported as volumetric water content. Errors calculated in the manuscript
24 are absolute errors in volumetric water content between the soil moisture probe data and the values derived from
25 analysis of the GPR data.

26 Errors in the estimation of volumetric water content from the simulated and measured GPR data vary over space and
27 time. The authors offer explanations for these errors which will be the focus of later research, e.g. evidence of non-
28 uniform wetting of the sand from soil moisture probe data and migration artifacts present in the Kirchoff migration.
29 The authors do not recommend directly comparing results of this method to those of cross-hole GPR given increased
30 data coverage using cross-hole GPR methods. The appeal of this method is partially because boreholes are not required
31 to image the subsurface.

32 *ARI: Finally, as much as I like GPR, it should be clearly stated in the introduction that GPR can only be used in*
33 *relatively resistive soil conditions. This is generally omitted when presenting GPR applications, yet in many practical*
34 *situations the soil conductivity is high enough to force us to shift to ERT or EMI for soil moisture content estimates.*

35 **Author Response:** The authors have added a statement to the introduction that describes the limitations of GPR in
36 conductive media.

37 **Author Response to Interactive comment on “Reflection tomography of time-lapse GPR data for studying dynamic**
38 **unsaturated flow phenomena” by Adam R. Mangel et al.**

39 This response is directed toward the comments left by Anonymous Referee #2, posted to the Hydrology and Earth
40 Systems Sciences (HESS) discussion board for manuscript [hess-2018-230](#) on October 23, 2018.

41 First and foremost, the authors would like to thank Anonymous Referee #2 (AR2) for devoting time to reviewing our
42 manuscript and for providing a critical review of the content. Below, the authors have outlined responses to individual
43 comments made by the reviewer.

44 **AR2:** *In section 2.2, line 128, authors mention that 101 CMPs were collected (between $y=1\text{m}$ and $y=3\text{m}$). I think there*
45 *must be a typo here. It should “COPs.” Otherwise, it does not make sense. If the transmitter and the receiver have*
46 *moved 2cm each time, you should have 51 profiles. If each one has moved 1cm at a time, then you will have 101*
47 *profiles. Please fix and/or clarify.*

48 **Author Response:** The discussion of the data collection geometry in the manuscript has been reviewed by the
49 corresponding author and is correct. A common-midpoint profile (CMP) was collected at 101 individual points
50 between $y = 1 \text{ m}$ and $y = 3 \text{ m}$ (see Figure 1f in the manuscript). To collect a CMP, the transmitter and receiver are
51 expanded or contracted about a central point. The central point locations are spaced at 2 cm intervals along the line at
52 $x = 2 \text{ m}$ over the distance of $y = 1$ to 3 m. Therefore, the total transect distance of 2 meters ($3 \text{ m} - 1 \text{ m}$) is covered in
53 100 steps of 2 cm increments. Counting the starting position, this calculates to a total of 101 CMPs.

54 Of course, you could rearrange the data to give you multiple common offset profiles across the tank. The number of
55 COPs in this case would depend on the number of offsets collected in each CMP, which for this experiment was 84.
56 These COPs, however, would be collected with significant temporal disparity such that the traces at either end of the
57 COP would be separated in time by 3.9 minutes. This would distort the reflectors in the COPs due to the dynamic
58 nature of the infiltration process being monitored. The COPs are of little value to our work, however, as they do not
59 contain the reflector moveout relationships that are used to estimate wave velocities. Thus, we only collected data in
60 CMP configurations.

61 **AR2:** *It is mentioned that the flux is 0.125 cm/min, but the authors did not explain how uniform the irrigation was*
62 *(inside the irrigation area).*

63 **Author Response:** Lines 104-105 of the manuscript mention heterogeneity in the applied flux. This
64 may indeed be a factor in the heterogeneity of the wetting front, but we have gone through many
65 iterations of the irrigation equipment to minimize the problem and have made progress in
66 homogenizing the applied flux over a prescribed area. While we continue to work on this issue, it
67 does not impact the validity of our results give that we do not fundamentally assume homogeneity
68 of the infiltration flux across the tank for reflection tomography to be applicable. To the contrary,
69 our GPR and moisture probe results are both consistent with some degree of variability occurring
70 in the applied flux. For this work, we feel that homogeneous application of water at the surface is
71 less important than the fact that we are able to discriminate a heterogeneous response, which is
72 more representative of real systems and points to the capability of reflection tomography for
73 measuring heterogeneous water distributions in the environment.

74

75 *AR2: The moisture probes were situated 0.5 m away from the line of GPR scan. Unless, the irrigation was uniform,*
76 *it does not make sense to compare the results of moisture content from the GPR scans to moisture content data from*
77 *the probes. I guess, we assume the sand layer was homogeneous.*

78 **Author Response:** The sand layer is homogeneous, meaning that it is all the same sand, from the same company, and
79 was packed into the tank in a uniform manner. However, homogenous systems can exhibit heterogeneous flow
80 responses due to small variabilities in initial and boundary conditions or very minor contrasts in sorting at the grain
81 scale. The overall agreement between the patterns of water content change observed in the reflection tomography and
82 probe responses suggest that the general comparison between the datasets we performed is valid, though we agree
83 with the reviewer that over analysis of the two data sets is not warranted given this limiting factor as well as the fact
84 that the measurements represent different scales of investigation.

85 The moisture probes were located off the GPR transect to avoid backscattering or the transmitted signal that would
86 interfere with analysis of the GPR wave velocities. Though this is not an ideal setup for comparison of the moisture
87 probe data to the GPR estimated of water content, it was necessary to ensure that high-quality reflection tomography
88 data could be collected.

89 *AR2: In line 183, it is mentioned that a refraction is also observed on the CMPs. Please discuss and explain why*
90 *refraction happened in this case.*

91 **Author Response:** Refraction occurs in this case because a wet low-velocity layer is present above a dry high-velocity
92 layer. Overall, the refraction is irrelevant to this work, but the authors point it out as a rarity in the simulated GPR
93 data. The refraction is not observed in the empirical GPR data and warrants no further discussion.

94 *AR2: In section 4, line 225, the error was reported for water content near the edges of the advancing plume. Please*
95 *explain how the errors were calculated considering the fact that the GPR scans were collected at fixed $x=2.0$ m and*
96 *the probes are 0.5 m away from the line of scan. How did you calculate the water content error for the central area*
97 *versus the edges of the plume. Please explain.*

98 **Author Response:** Errors in the estimates of water content are calculated by comparing the difference between the
99 soil moisture probe data and the values derived from analysis of the GPR data. We must assume homogeneity in the
100 x-direction to directly compare these measurements which is why the errors are not discussed in greater detail in this
101 work. Rather, the authors provide these numbers as a general metric regarding the performance of the GPR data
102 analysis.

103

Reflection tomography of time-lapse GPR data for studying dynamic unsaturated flow phenomena

Adam R. Mangel^{1,2}, Stephen M.J. Moysey², John Bradford¹

¹ Department of Geophysics, Colorado School of Mines, Golden, Colorado, 80401, USA

² Department of Environmental Engineering and Earth Science, Clemson University, Clemson, South Carolina, 29634, USA

Corresponding to: Adam R. Mangel (amangel@mines.edu)

Abstract

Ground-penetrating radar (GPR) reflection tomography algorithms allow non-invasive monitoring of water content changes resulting from flow in the vadose zone. The approach requires multi-offset GPR data that is traditionally slow to collect. We automate GPR data collection to reduce the survey time significantly, thereby making this approach to hydrologic monitoring feasible. The method was evaluated using numerical simulations and laboratory experiments that suggest reflection tomography can provide water content estimates to within 5-10% vol./vol. for the synthetic studies, whereas the empirical estimates were typically within 5-15% of measurements from in-situ probes. Both studies show larger observed errors in water content near the periphery of the wetting front, beyond which additional reflectors were not present to provide data coverage. Overall, coupling automated GPR data collection with reflection tomography provides a new method for informing models of subsurface hydrologic processes and a new method for determining transient 2D soil moisture distributions.

1. Introduction

Preferential flow is ubiquitous in the vadose zone, occurring under a wide variety of conditions and over a broad range of scales (Nimmo, 2012). Reviews such as those by Hendrickx and Flury (2001) and Jarvis (2007) illustrate that a basic mechanistic understanding of preferential flow exists. Jarvis et al. (2016) point out, however, that we still lack models capable of reproducing empirical observations in the field and highlight the importance of non-invasive imaging techniques for improving this understanding. We suggest that ground-penetrating radar (GPR) reflection tomography could fill this need by quantitatively mapping changes in water content through space and time at the sub-meter scale.

Reflection GPR is commonly used to image subsurface structures, but is also well suited to understanding hydrologic variability due to the strong dependence of EM wave velocities on soil volumetric water content (Topp et al., 1980). As a result, GPR has been adapted to monitor variability in hydrologic processes at multiple scales through time and space in a variety of contexts (Buchner et al., 2011; Busch et al., 2013; Guo et al., 2014; Haarder et al., 2011; Lunt et al., 2005; Mangel et al., 2012, 2015b, 2017; Moysey, 2010; Sautenoy et al., 2007; Steelman and Endres, 2010; Vellidis et al., 1990). Note that GPR methods are not applicable in media with relatively high electrical conductivity.

While these studies have illustrated a variety of techniques for monitoring changes in water content within the subsurface, they have generally required assumptions to constrain the interpretation, such as the use of *a priori* information regarding subsurface structure (e.g., Lunt et al., 2005) or the GPR wave velocity (Haarder et al., 2011).

140 These limitations arise from the fact that GPR data are recorded as energy arriving at the receiver antenna as a function
141 of time. Inherent assumptions therefore exist in analyzing traveltime data collected with antennas separated by a fixed
142 offset because both the distance travelled by the GPR wave to a reflector and the velocity of the GPR wave are
143 unknown. It has been demonstrated that GPR data collected via a multi-offset survey can constrain both the depth to
144 a moving wetting front and the water content behind the front over the course of an infiltration event (Gerhards et al.,
145 2008; Mangel et al., 2012). The limitation of these studies, however, was that the authors assumed a 1D flow system
146 and that GPR data lacked information regarding lateral variability in soil moisture.

147 Extending multi-offset techniques (Forte and Pipan, 2017; Jaumann and Roth, 2017; Klenk et al., 2015;
148 Lambot et al., 2004, 2009) to image flow in the vadose zone requires an increase in the speed at which these data can
149 be collected and advanced processing methods that can combine thousands of measurements into spatially and
150 temporally variable water content estimates. We have recently overcome the data collection problem by automating
151 GPR data collection using a computer controlled gantry, thereby reducing the data collection time for large multi-
152 offset surveys from hours to minutes (Mangel et al., 2015a). ~~Reflection tomography and wave migration~~ algorithms
153 ~~from seismic literature~~ have been available ~~in the seismic industry~~ for decades (Baysal et al., 1983; Lafond and
154 Levander, 1993; Sava and Biondi, 2004a, 2004b; Stork, 1992; Yilmaz and Chambers, 1984) and ~~were first~~ ~~are being~~
155 ~~continually~~ adapted to ~~imaging~~ GPR applications. ~~For example, this work is made possible due to a velocity variations~~
156 ~~by Bradford (2006)~~ ~~daptation of the pre-stack migration algorithm~~ (Leparoux et al., 2001) ~~and adaptation of the~~
157 ~~reflection tomography algorithm~~ (Bradford, 2006) ~~to multi-offset GPR data~~. Subsequent studies have demonstrated
158 the use of GPR reflection tomography for imaging static distributions of subsurface water content with great detail
159 (Bradford, 2008; Bradford et al., 2009; Brosten et al., 2009). The combination of automated GPR data collection and
160 reflection tomography makes time-lapse imaging of water content during infiltration a feasible means to study flow
161 in the vadose zone.

162 The objective of this study is to evaluate reflection tomography of high-resolution GPR data as a tool for
163 observing and characterizing unsaturated flow patterns during infiltration into a homogeneous soil. To evaluate the
164 efficacy of the algorithm for resolving dynamic soil water content in 2D, we first test the algorithm using numerical
165 simulations and compare the results to true water content distributions. We then apply the algorithm to time-lapse
166 GPR data collected during an infiltration and recovery event in a homogeneous soil and compare results to
167 measurements from in-situ soil moisture probes.

168 2. Methods

169 2.1. The Reflection Tomography Algorithm

170 The goal of reflection tomography is to determine a velocity model that best aligns migrated reflection
171 arrivals for a common reflection point across a set of source-receiver offsets. For brevity, we will limit our discussion
172 here to the key ideas and methods of the tomography algorithm; we refer the reader to Stork (1992) for the original
173 tomography algorithm and to Bradford (2006) for the application to GPR data.

174 The data required for this algorithm are an ensemble of common-midpoint (CMP) gathers collected along a
175 path. Given that GPR data is a time-series record of electromagnetic energy arriving at a point in space, we must
176 know the proper velocity structure to migrate the data and produce a depth registered image of the GPR energy.

177 Migration attempts to remove the hyperbolic trend of reflections with respect to antenna offset (Figure 1a) by using
178 the wave velocity to reposition reflections to the proper depth at which they occur. If CMP data are migrated with the
179 correct velocity, reflections from layers in the subsurface are flattened as a function of offset (Fig. 1c). If the velocity
180 estimate is incorrect, e.g. 10% too slow (Fig. 1b) or 10% too fast (Fig. 1d), the arrival is not flat and exhibits residual
181 moveout (RMO). To solve for the velocity structure and properly migrate the data, the reflection tomography
182 algorithm proceeds as follows (Bradford, 2006; Stork, 1992):

- 183 1. Generate a starting depth vs. velocity model.
- 184 2. Migrate the data with the starting velocity model and stack the data.
- 185 3. Pick horizons on the stacked image.
- 186 4. Perform ray-tracing to the picked horizons with the velocity model.
- 187 5. Evaluate horizons for residual moveout.
- 188 6. Adjust velocity model using reflection tomography.
- 189 7. Apply revised velocity model using migration and quality check RMO.
- 190 8. Iterate at step three if necessary.

191 For this work, starting velocity models for the tomography algorithm are determined by smoothing results
192 from 1D velocity analysis of individual CMPs (Neidell and Taner, 1971). The reflection tomography algorithm then
193 adjusts the velocity distribution until reflections in the depth corrected (i.e., migrated) data line up to produce a
194 reflection at a consistent depth across all traces in a CMP. Through sequential iterations of the tomographic inversion,
195 the RMO metric is reduced on a global scale. For this work, the reflection tomography was performed using the
196 SeisWorks software suite and Kirchhoff pre-stack depth migration (Yilmaz and Doherty, 2001).

197 **2.2. Experimental Setup and Procedure**

198 We used a 4 m x 4 m x 2 m tank for the controlled study of unsaturated flow phenomenon with GPR (Fig.
199 1e, f). We filled the tank with a medium-grained sand to a depth of 0.60 m. Below the sand was a 0.30 m layer of
200 gravel that acts as backfill for 16 individual drain cells that are pitched slightly toward central drains that route water
201 to outlets on the outside of the tank. We constructed an automated data collection system to allow for the high-speed
202 high-resolution collection of GPR data (Mangel et al., 2015a); the GPR gantry fits inside of the tank so the antennas
203 are in contact with the sand surface. All GPR data described here were collected along the y-axis of the tank at a fixed
204 position of $x = 2.0$ m, where the bottom of the tank is flat (Fig. 1e, f).

205 The automated system, which utilizes a 1000 MHz Sensors and Software bistatic radar (Sensors and
206 Software, Inc.), was operated to obtain 101 CMPs spaced at 0.02 m intervals between $y = 1.0 - 3.0$ m. Each CMP
207 consisted of 84 traces with offsets between 0.16-1.0 m at 0.01 m step size. Thus, a complete CMP data set for one
208 observation time consists of almost 8,500 individual GPR traces. With this configuration using the automated system,
209 a CMP at a single location could be collected in 1.8 seconds with a total cycle of CMP data locations collected every
210 3.9 minutes.

211 GPR data collection occurred prior to irrigation to evaluate background conditions. Data collection continued
212 during irrigation, which was applied at a flux of 0.125 cm/min for a duration of 2.13 hrs. Spatial heterogeneity in the
213 applied flux has been observed in laboratory testing of the irrigation equipment. Fifteen EC-5 soil moisture probes

214 (METER, Inc.) logged volumetric water content at 10 second intervals during the experiment (Fig. 1e, f). Note that
215 the soil moisture probes are located out of the plane of the GPR line by 0.5 m (Figure 1f). GPR data collection
216 continued for 40 min. after the irrigation was terminated. In total, 45 complete sets of data were collected over the
217 course of the 3-hour experiment, yielding more than 500,000 GPR traces in the experimental data set.

218 **2.3. Execution of the Numerical Simulations**

219 We employed HYDRUS-2D (Simunek and van Genuchten, 2005) to simulate a theoretical and realistic
220 hydrologic response to an infiltration event using two different initial conditions: i) hydrostatic equilibrium leading to
221 a water content distribution controlled by the soil water retention curve, and ii) a uniform soil with a water content of
222 0.07. We selected the Mualem-van Genuchten soil model (Mualem, 1976) and parameterized the model as follows
223 based on hydraulic testing of the sand: residual water content (θ_r) = 0.06, saturated water content (θ_s) = 0.38, air-entry
224 pressure (α) = 0.058 cm⁻¹, shape parameter (n) = 4.09, and saturated hydraulic conductivity (K_s) = 4.6 cm min⁻¹. The
225 hydraulic conductivity for the homogeneous model was reduced to 1 cm min⁻¹ to build a larger contrast of water
226 content across the wetting front. For all HYDRUS simulations, we used a constant flux boundary condition of 0.125
227 cm/min from $y = 1.6 - 2.4$ m along the ground surface, set the model domain depth to 0.6 m, length to 4.0 m, and
228 nominal cell size to 0.04 m. Remaining nodes at the surface were set to no flow boundaries and lower boundary nodes
229 were set to a seepage face with the pressure head equal to zero.

230 We calculated relative dielectric permittivity values for the GPR simulations by transforming water content values
231 from HYDRUS-2D using the Topp equation (Topp et al., 1980). We used the magnetic permeability of free space for
232 the entire model domain and set electrical conductivity of the soil to 1 mS/m. Although electrical conductivity changes
233 as a function of the water content, these changes primarily influence wave attenuation, which is not significant or
234 accounted for in the processing performed with the SeisWorks software.

235 We performed GPR simulations in MATLAB using a 2D finite-difference time-domain code (Irving and
236 Knight, 2006). The GPR model domain was set to 4.0 m long and 1.1 m high with a cell size of 0.002 m. The lower
237 0.3 m of the domain was set to a relative dielectric permittivity of 2.25 to represent the lower gravel layer and the
238 upper 0.2 m was modeled as air to simulate the air-soil interface. Simulated data were collected as described in the
239 section detailing the tank experiment. For quick computation, simulations were deployed on the Palmetto
240 supercomputer cluster at Clemson University, where single source simulations ran in 20 minutes using nodes with 8
241 CPUs and 32 GB of RAM.

242 **3. Reflection Tomography of Simulations**

243 The HYDRUS-2D output shows the development of an infiltrating wetting front for the two scenarios with
244 differing initial conditions (Figs. 2a, f, k). For conditions prior to irrigation, the bottom of sand reflection (B) is
245 horizontal on the common-offset profile (COP) data indicating a constant velocity across the model domain (Fig. 2b).
246 Additionally, the CMPs show identical hyperbolic moveout, i.e., the offset vs. travelttime relationship, indicating a
247 homogeneous velocity across the model domain (Fig. 2c-e). The airwave and groundwave are also visible in the data,
248 but are not analyzed, or further discussed.

249 During infiltration, (B) is distorted at the center of the COP due to the decreased velocity caused by the
250 infiltrating water (Figs. 2g, l). A reflection from the infiltrating wetting front (W) is faintly visible for the model with

251 variable initial water contents (Fig. 2g) and comparatively strong for simulations with a dry background (Fig. 2l) due
252 to different levels of dielectric contrast across the wetting front in each case. CMPs also indicate perturbations in the
253 velocity field as the moveout changes dramatically when the wetted zone is encountered (Figs. 2h-j, m-o). A refraction
254 is also observed on the CMPs, which is a rare occurrence considering that GPR wave velocity typically decreases with
255 depth.

256 Prior to the onset of flow, the reflection tomography algorithm produces a uniform water content distribution
257 that agrees with the arithmetic average of the true water content but does not capture the vertical gradation observed
258 in Figure 3a. This is because information regarding vertical velocity variations is absent, i.e., more reflectors at
259 different depths are required to capture this variability. As a result, errors in the water content estimation exceed 10%
260 vol./vol (Fig. 3c).

261 During infiltration the wetting front is imaged relatively well for the case where the soil was initially dry
262 (Figs. 3g-i), particularly as the plume advances deeper into the subsurface (Figs. 3j-l) where there is improved data
263 coverage. Considerable errors in the tomography results persist, however, with the results degrading further for the
264 scenario with variable initial water content (Figs. 3d-f) given that reflection contrasts with the wetting front are weaker.
265 The presence of an additional reflector, however, increases the ability of the tomography to resolve vertical variability,
266 e.g. Figure 2e vs. Figure 2b. Overall, errors are reduced near reflectors to about 5% vol./vol. These results suggest
267 that water content changes resulting from unsaturated flow can be imaged and that as more information becomes
268 available in the form of additional reflections, the tomography results improve.

269 4. Reflection Tomography of Experimental Data

270 At initial conditions, the sand layer reflection (B) is visible at 10 ns traveltimes in the COP collected over the
271 imaging area (Fig. 4a). Normal hyperbolic moveout of (B) is observed on the CMPs (Fig. 4b, c, d). These results are
272 qualitatively identical to observations from numerical simulations (Figs. 2b-e).

273 During infiltration, the water content of the sand layer increases substantially (Fig. 5) and longer traveltimes
274 of the arrivals on the COP data are observed near the center of the tank (Figs. 4f, i). Rather than a coherent reflection
275 for the wetting front (W) (Fig. 2l), multiple discrete reflections are present in the COP data (Fig. 4e, i, m) indicating
276 a heterogeneous wetting of the soil. These reflections are difficult to identify on the CMPs given the complex moveout
277 pattern (Fig. 4i) but are more easily identified in animations of COP projections of the data (included as a
278 supplementary file). Analysis of the data was greatly aided by the animation of the data and the pre-stack migration
279 algorithm, which stacks the data over all offsets to produce a coherent image of reflectors with an increased signal to
280 noise ratio. Heterogeneous wetting of the soil is also very pronounced in the soil-moisture probe data with many of
281 the probes responding out of sequence with depth (Fig 5). After irrigation, the soil moisture probes show a decrease
282 in the soil water content (Fig. 5) apart from one probe (Fig. 5c) and the GPR data show a slight decrease in the
283 traveltimes of the bottom of sand reflection (Figs. 4k-n).

284 The tomographic imaging results from the initial GPR data set collected prior to irrigation agree with data
285 from soil moisture probes which indicates an average soil moisture of roughly 5% during this time (Figs. 4e, 5).
286 During infiltration and recovery, tomographic images of the tank show a wet zone at the center and relatively dry
287 edges outside the irrigated area (Figs. 4j, o). Overall, the tomography results near the center of the tank are within

288 10% vol./vol. of the soil moisture data and show a non-uniform wetting of the soil during infiltration that was not
289 observed in the numerical study, suggesting the occurrence of preferential flow. Errors in the estimates of water
290 content near the edges of the advancing plume exceed 15% vol./vol. (Fig. 4b, c), though the general patterns in wetting
291 are consistent. After irrigation, the tomography results on the edges of the wetted zone are in better agreement with
292 the soil moisture probe data, but less spatial information is available given the lack of a wetting front reflection (Fig.
293 4o).

294 **5. Conclusions**

295 Reflection tomography in the post-migrated domain is a viable method for resolving transient soil moisture
296 content in 2D associated with an infiltration and recovery event in a homogeneous soil. Reflection tomography of
297 numerical data produced water content distributions that were in good agreement with true water content values from
298 the simulations. The tomography was generally able to match the true water content values to within 5-10% vol. /vol.
299 However, distinct migration artifacts were produced around the edges of the wetting front, especially for cases where
300 the initial water content was non-uniform, obscuring details about the shape of the wetted region. Analysis of data
301 collected in a sand tank proved to be more difficult, however, the tomography was able to produce hydrologically
302 realistic distributions of water content in space and time that were generally within 5-15% vol./vol. of measurements
303 from in-situ soil moisture probes. This may have to do with the complex distribution of the wetted soil as a result of
304 heterogenous distribution of water at the surface, texture variability in the soil, or other preferential flow mechanisms
305 (Jarvis et al., 2016). Regardless, the fact that the GPR data were able to capture this heterogeneity is an impressive
306 feat given that tomographic imaging operated independently of any hydrologic information and provided evidence
307 that our conceptual model was not representative of the physical system.

308 Regardless of discrepancies observed between the GPR and probe water content values, it is evident that
309 automated high-speed GPR data acquisition coupled with reflection tomography algorithms can provide a new
310 approach to hydrologic monitoring. Testing and revision of conceptual hydrologic models regarding non-uniform
311 flow in the vadose zone demands such non-invasive time-lapse imaging data. Artifacts observed in the numerical
312 simulation results, however, suggest that improvements in this methodology could be achieved. While there are likely
313 fundamental limitations to the information content of the data, the Kirchhoff pre-stack depth migration algorithm used
314 in this study could be replaced by more sophisticated algorithms like reverse-time migration (Baysal et al., 1983)
315 which may reduce the observed imaging artifacts. Additionally, results from the tomography algorithm may prove to
316 be beneficial as a precursor to higher-order inversion techniques, like full-waveform inversion, which requires detailed
317 starting models of velocity for convergence. Overall, coupling automated GPR data collection with reflection
318 tomography provides a new method for informing models of subsurface hydrologic processes and a new method for
319 determining transient 2D soil moisture distributions.

320 **6. Acknowledgements**

321 This material is based upon work supported by, or in part by, the National Science Foundation under grant
322 number EAR-1151294. We also acknowledge Clemson University for generous allotment of compute time on

323 Palmetto cluster. Data used in this publication and a supplementary movie of the data are available through the
324 Colorado School of Mines at the following URL: <https://hdl.handle.net/11124/172053>.
325

326 **7. References**

- 327 Baysal, E., Kosloff, D. and Sherwood, J.: Reverse Time Migration, *Geophysics*, 48(11), 1514–1524,
328 doi:10.1190/1.1441434, 1983.
- 329 Bradford, J. H.: Applying reflection tomography in the postmigrated domain to multifold ground-penetrating radar
330 data, *Geophysics*, 71(1), K1–K8, doi:10.1190/1.2159051, 2006.
- 331 Bradford, J. H.: Measuring Water Content Heterogeneity Using Multifold GPR with Reflection Tomography, *Vadose*
332 *Zo. J.*, 7(1), 184, doi:10.2136/vzj2006.0160, 2008.
- 333 Bradford, J. H., Clement, W. P. and Barrash, W.: Estimating porosity with ground-penetrating radar reflection
334 tomography: A controlled 3-D experiment at the Boise Hydrogeophysical Research Site, *Water Resour. Res.*, 45(4),
335 n/a-n/a, doi:10.1029/2008WR006960, 2009.
- 336 Brosten, T. R., Bradford, J. H., McNamara, J. P., Gooseff, M. N., Zarnetske, J. P., Bowden, W. B. and Johnston, M.
337 E.: Multi-offset GPR methods for hyporheic zone investigations, *Near Surf. Geophys.*, 7, 244–257, 2009.
- 338 Buchner, J. S., Kuhne, A., Antz, B., Roth, K. and Wollschläger, U.: Observation of volumetric water content and
339 reflector depth with multichannel ground-penetrating radar in an artificial sand volume, 2011 6th Int. Work. Adv. Gr.
340 Penetrating Radar, 1–5, doi:10.1109/IWAGPR.2011.5963910, 2011.
- 341 Busch, S., Weihermüller, L., Huisman, J. A., Steelman, C. M., Endres, A. L., Vereecken, H. and van der Kruk, J.:
342 Coupled hydrogeophysical inversion of time-lapse surface GPR data to estimate hydraulic properties of a layered
343 subsurface, *Water Resour. Res.*, 49(12), 8480–8494, doi:10.1002/2013WR013992, 2013.
- 344 Forte, E. and Pipan, M.: Review of multi-offset GPR applications: Data acquisition, processing and analysis, *Signal*
345 *Processing*, 132, 1–11, doi:10.1016/j.sigpro.2016.04.011, 2017.
- 346 Gerhards, H., Wollschläger, U., Yu, Q., Schiewek, P., Pan, X. and Roth, K.: average soil-water content with
347 multichannel ground-penetrating radar, , 73(4), 15–23, 2008.
- 348 Guo, L., Chen, J. and Lin, H.: Subsurface lateral preferential flow network revealed by time-lapse ground-penetrating
349 radar in a hillslope, *Water Resour. Res.*, 50, 9127–9147, doi:10.1002/2013WR014603, 2014.
- 350 Haarder, E. B., Looms, M. C., Jensen, K. H. and Nielsen, L.: Visualizing Unsaturated Flow Phenomena Using High-
351 Resolution Reflection Ground Penetrating Radar, *Vadose Zo. J.*, 10(1), 84, doi:10.2136/vzj2009.0188, 2011.
- 352 Hendrickx, J. M. H. and Flury, M.: Uniform and Preferential Flow Mechanisms in the Vadose Zone, in *Conceptual*
353 *Models of Flow and Transport in the Fractured Vadose Zone*, pp. 149–187, National Academy Press, Washington,
354 D.C., 2001.
- 355 Irving, J. and Knight, R.: Numerical modeling of ground-penetrating radar in 2-D using MATLAB, *Comput. Geosci.*,
356 32(9), 1247–1258, doi:10.1016/j.cageo.2005.11.006, 2006.
- 357 Jarvis, N., Koestel, J. and Larsbo, M.: Understanding Preferential Flow in the Vadose Zone: Recent Advances and
358 Future Prospects, *Vadose Zo. J.*, 15(12), 0, doi:10.2136/vzj2016.09.0075, 2016.
- 359 Jarvis, N. J.: A review of non-equilibrium water flow and solute transport in soil macropores: Principles, controlling
360 factors and consequences for water quality, *Eur. J. Soil Sci.*, 58(3), 523–546, doi:10.1111/j.1365-2389.2007.00915.x,
361 2007.
- 362 Jaumann, S. and Roth, K.: Soil hydraulic material properties and subsurface architecture from time-lapse GPR,

363 Hydrol. Earth Syst. Sci. Discuss., (September), 1–34, doi:10.5194/hess-2017-538, 2017.

364 Klenk, P., Jaumann, S. and Roth, K.: Quantitative high-resolution observations of soil water dynamics in a complicated
365 architecture using time-lapse ground-penetrating radar, *Hydrol. Earth Syst. Sci.*, 19(3), 1125–1139, doi:10.5194/hess-
366 19-1125-2015, 2015.

367 Lafond, C. F. and Levander, A. R.: Migration moveout analysis and depth focusing, *Geophysics*, 58(1), 91–100,
368 doi:10.1190/1.1443354, 1993.

369 Lambot, S., Antoine, M., van den Bosch, I., Slob, E. C. and Vanclooster, M.: Electromagnetic Inversion of GPR
370 Signals and Subsequent Hydrodynamic Inversion to Estimate Effective Vadose Zone Hydraulic Properties, *Vadose*
371 *Zo. J.*, 3(4), 1072, doi:10.2136/vzj2004.1072, 2004.

372 Lambot, S., Slob, E., Rhebergen, J., Lopera, O., Jadoon, K. Z. and Vereecken, H.: Remote Estimation of the Hydraulic
373 Properties of a Sand Using Full-Waveform Integrated Hydrogeophysical Inversion of Time-Lapse, Off-Ground GPR
374 Data, *Vadose Zo. J.*, 8(3), 743, doi:10.2136/vzj2008.0058, 2009.

375 Leparoux, D., Gibert, D. and Cote, P.: Adaptation of prestack migration to multi-offset ground-penetrating radar
376 (GPR) data, *Geophys. Prospect.*, 49(3), 374–386, doi:10.1046/j.1365-2478.2001.00258.x, 2001.

377 Lunt, I. A., Hubbard, S. S. and Rubin, Y.: Soil moisture content estimation using ground-penetrating radar reflection
378 data, *J. Hydrol.*, 307(1–4), 254–269, doi:10.1016/j.jhydrol.2004.10.014, 2005.

379 Mangel, A. R., Moysey, S. M. J., Ryan, J. C. and Tarbutton, J. A.: Multi-offset ground-penetrating radar imaging of
380 a lab-scale infiltration test, *Hydrol. Earth Syst. Sci.*, 16(11), doi:10.5194/hess-16-4009-2012, 2012.

381 Mangel, A. R., Lytle, B. A. and Moysey, S. M. J.: Automated high-resolution GPR data collection for monitoring
382 dynamic hydrologic processes in two and three dimensions, *Lead. Edge*, 34(2), doi:10.1190/tle34020190.1, 2015a.

383 Mangel, A. R., Moysey, S. M. J. and van der Kruk, J.: Resolving precipitation induced water content profiles by
384 inversion of dispersive GPR data: A numerical study, *J. Hydrol.*, 525, 496–505, doi:10.1016/j.jhydrol.2015.04.011,
385 2015b.

386 Mangel, A. R., Moysey, S. M. J. and van der Kruk, J.: Resolving infiltration-induced water content profiles by
387 inversion of dispersive ground-penetrating radar data, *Vadose Zo. J.*, 16, doi:10.2136/vzj2017.02.0037, 2017.

388 Moysey, S. M.: Hydrologic trajectories in transient ground-penetrating-radar reflection data, *Geophysics*, 75(4),
389 WA211-WA219, doi:10.1190/1.3463416, 2010.

390 Mualem, Y.: A new model for predicting the hydraulic conductivity of unsaturated porous media, *Water Resour. Res.*,
391 12(3), 1976.

392 Neidell, N. S. and Taner, M. T.: Semblance and other coherency measures for multichannel data, *Geophysics*, 36(3),
393 482–497, 1971.

394 Nimmo, J. R.: Preferential flow occurs in unsaturated conditions, *Hydrol. Process.*, 26(5), 786–789,
395 doi:10.1002/hyp.8380, 2012.

396 Saintenoy, A., Schneider, S. and Tucholka, P.: Evaluating GroundPenetrating Radar use for water infiltration
397 monitoring, 2007 4th Int. Work. on, *Adv. Gr. Penetrating Radar*, 91–95, doi:10.1109/AGPR.2007.386531, 2007.

398 Sava, P. and Biondi, B.: Wave-equation migration velocity analysis. I. Theory, *Geophys. Prospect.*, 52(6), 593–606,
399 doi:10.1111/j.1365-2478.2004.00447.x, 2004a.

400 Sava, P. and Biondi, B.: Wave-equation migration velocity analysis — II : Subsalt imaging examples Geophysical
401 Prospecting , accepted for publication, , 1–36, 2004b.

402 Simunek, J. and van Genuchten, M. T.: HYDRUS code for simulating the movement of water, heat, and multiple
403 solutes in variably saturated porous media, 2005.

404 Steelman, C. M. and Endres, A. L.: An examination of direct ground wave soil moisture monitoring over an annual
405 cycle of soil conditions, *Water Resour. Res.*, 46(11), n/a-n/a, doi:10.1029/2009WR008815, 2010.

406 Stork, C.: Reflection tomography in the postmigrated domain, *Geophysics*, 57(5), 680–692, doi:10.1190/1.1443282,
407 1992.

408 Topp, G. C., Davis, J. L. and Annan, A. P.: Electromagnetic Determination of Soil Water Content:, *Water Resour.*
409 *Res.*, 16(3), 574–582, 1980.

410 Vellidis, G., Smith, M. C., Thomas, D. L. and Asmussen, L. E.: Detecting wetting front movement in a sandy soil
411 with ground-penetrating radar, *Am. Soc. Agric. Eng.*, 33(6), 1867–1874, 1990.

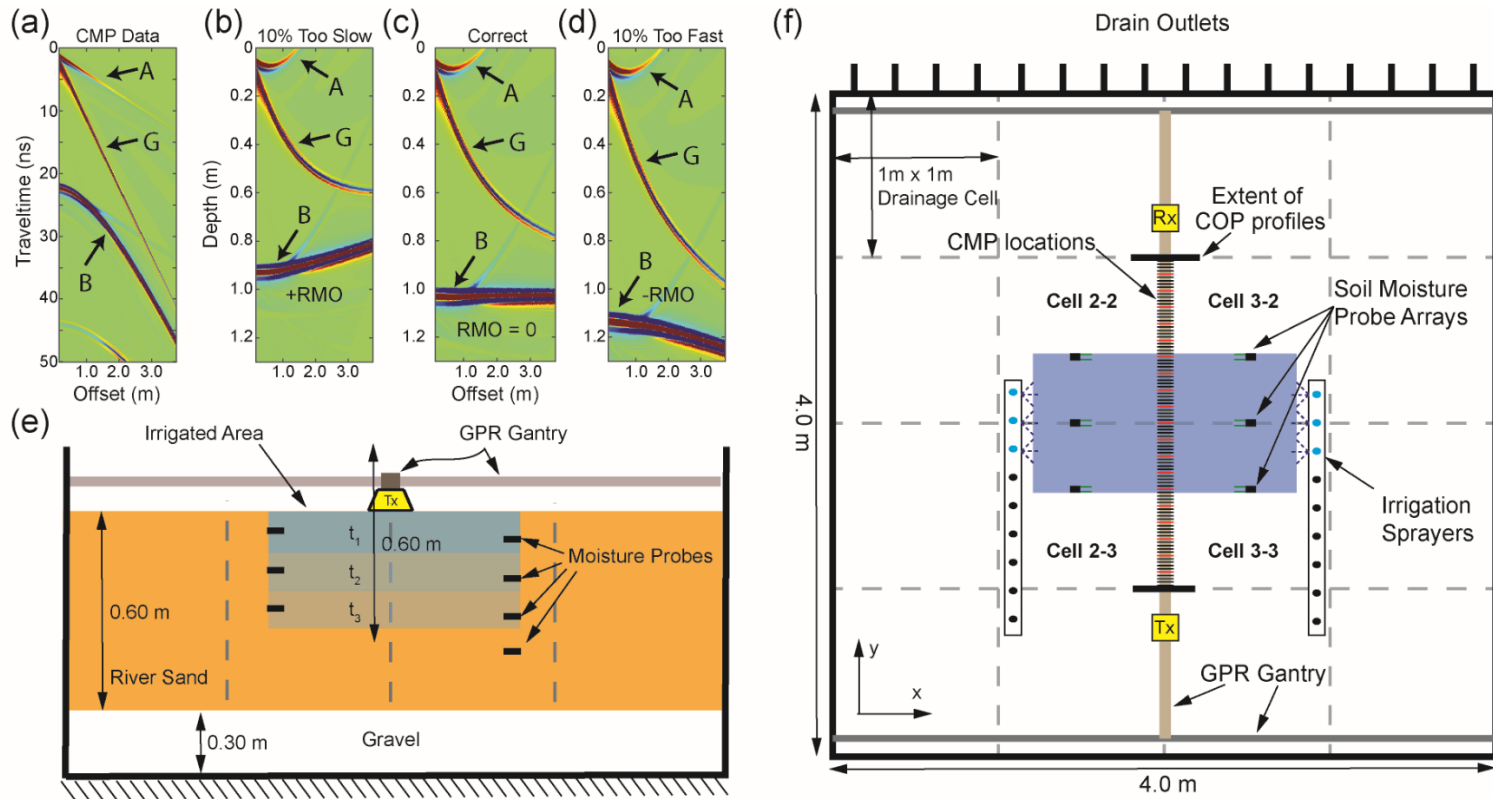
412 Yilmaz, O. and Chambers, R.: Migration velocity analysis by wave-field extrapolation, *Geophysics*, 49(10), 1664–
413 1674, 1984.

414 Yilmaz, O. and Doherty, S.: *Seismic Data Analysis: Processing, Inversion, and Interpretation of Seismic Data*, 2nd
415 ed., Society of Exploration Geophysicists, Tulsa, OK., 2001.

416

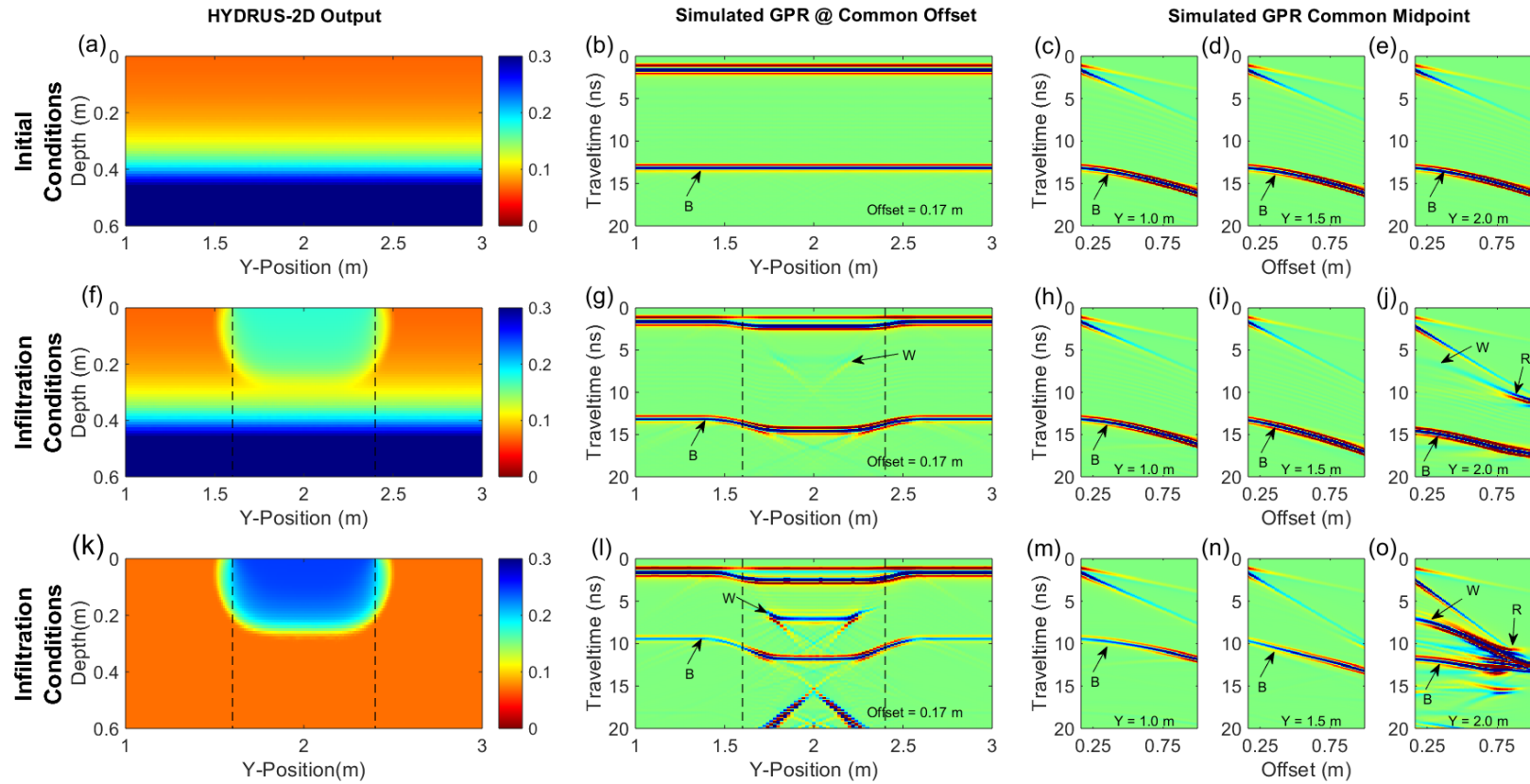
417 **8. Figures**

418 **Figure 1**



419

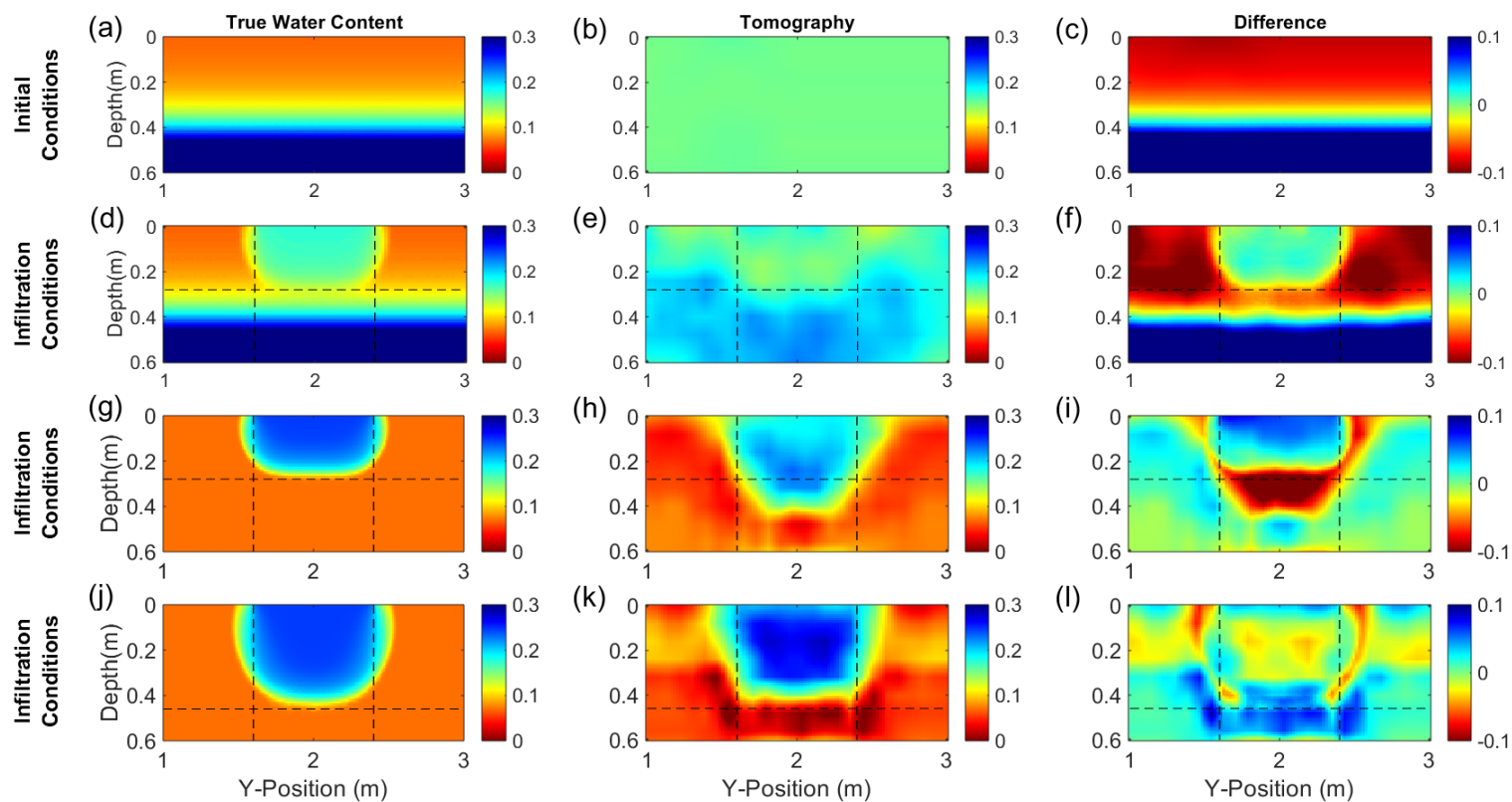
420 Figure 1: a) Example CMP data showing the airwave (A), groundwave (G) and reflection from a layer (B). Data in (a) is migrated to form (b) a migrated gather
 421 with velocity 10% slow; c) a migrated gather with correct velocity; and d) a migrated gather with velocity 10% fast. Panel (e) shows a cross-section of the experiment
 422 at $y = 2.0$ where t_1 , t_2 , and t_3 are arbitrary times during the infiltration. Panel (f) shows the plan-view of the experiment. Note that the bottom of the sand layer is
 423 flat where GPR data collection occurs, i.e. on a boundary between drain cells, and pitched elsewhere toward cell drains.



425

426 Figure 2: Panels (a), (f), and (k) show volumetric moisture distribution from HYDRUS-2D simulations used to generate simulated common-offset GPR data (b, g,
 427 l) and multi-offset GPR data (c-e, h-j, and m-o). Vertical dashed lines indicate the extent of the wetted surface. Annotated arrivals are the bottom of sand layer
 428 reflection (B), wetting front reflection (W), and refraction (R). Note that the base of sand reflection (B) is caused by the boundary at 0.60 m depth between the sand
 429 and gravel, not the capillary rise shown in panels (a) and (f).

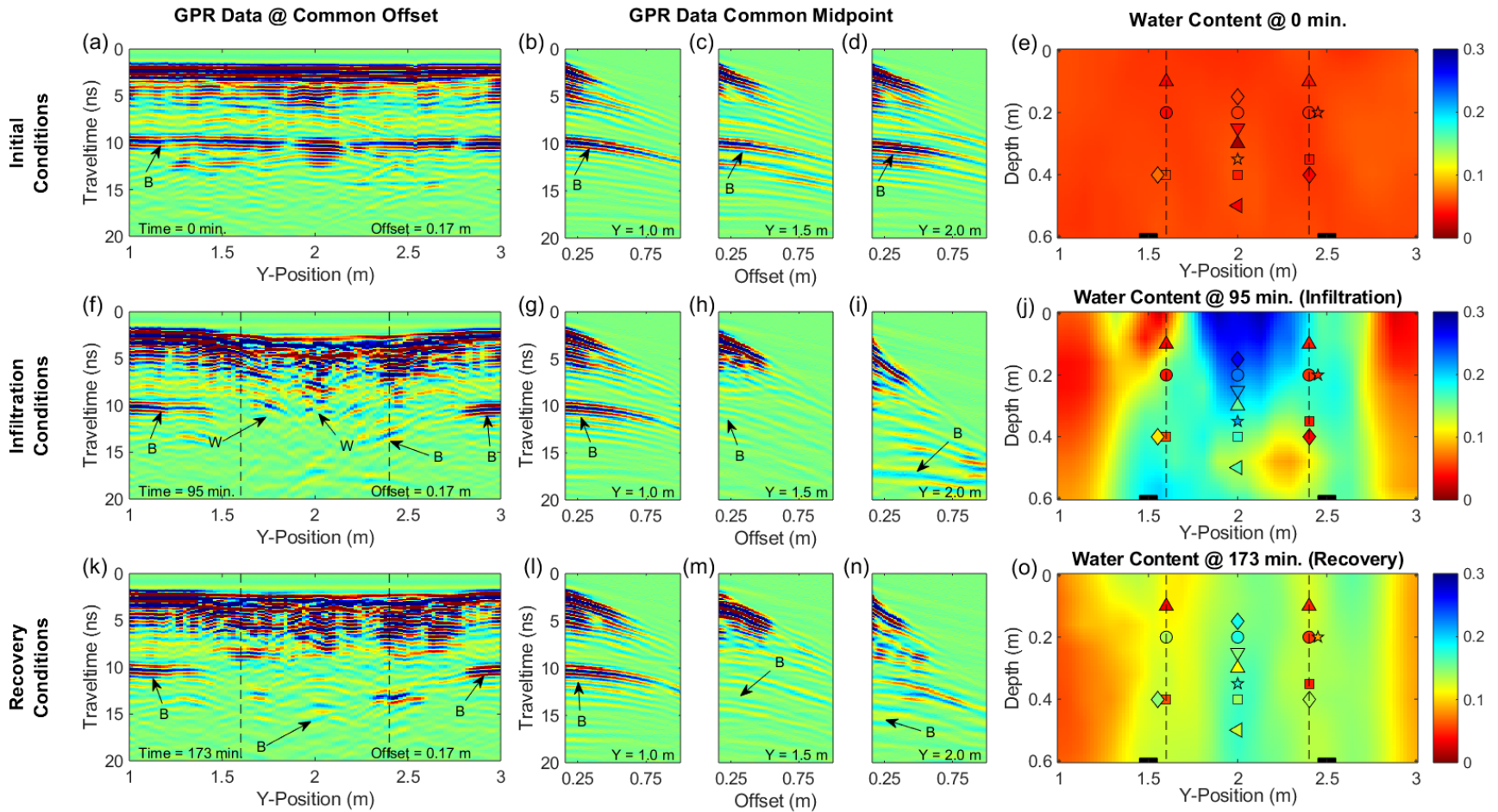
430 **Figure 3**



431

432 Figure 3: Panels (a), (d), (g), and (j) show true volumetric water content distributions from HYDRUS-2D. Panels (b), (e), (h), and (k) show results of tomography
433 of the simulated GPR data as volumetric water content. Difference plots (c), (f), (i), and (l) were calculated by subtracting the tomography results from the true
434 volumetric water content distributions; red areas indicate volumetric moisture underestimation while blue areas indicate volumetric moisture overestimation.

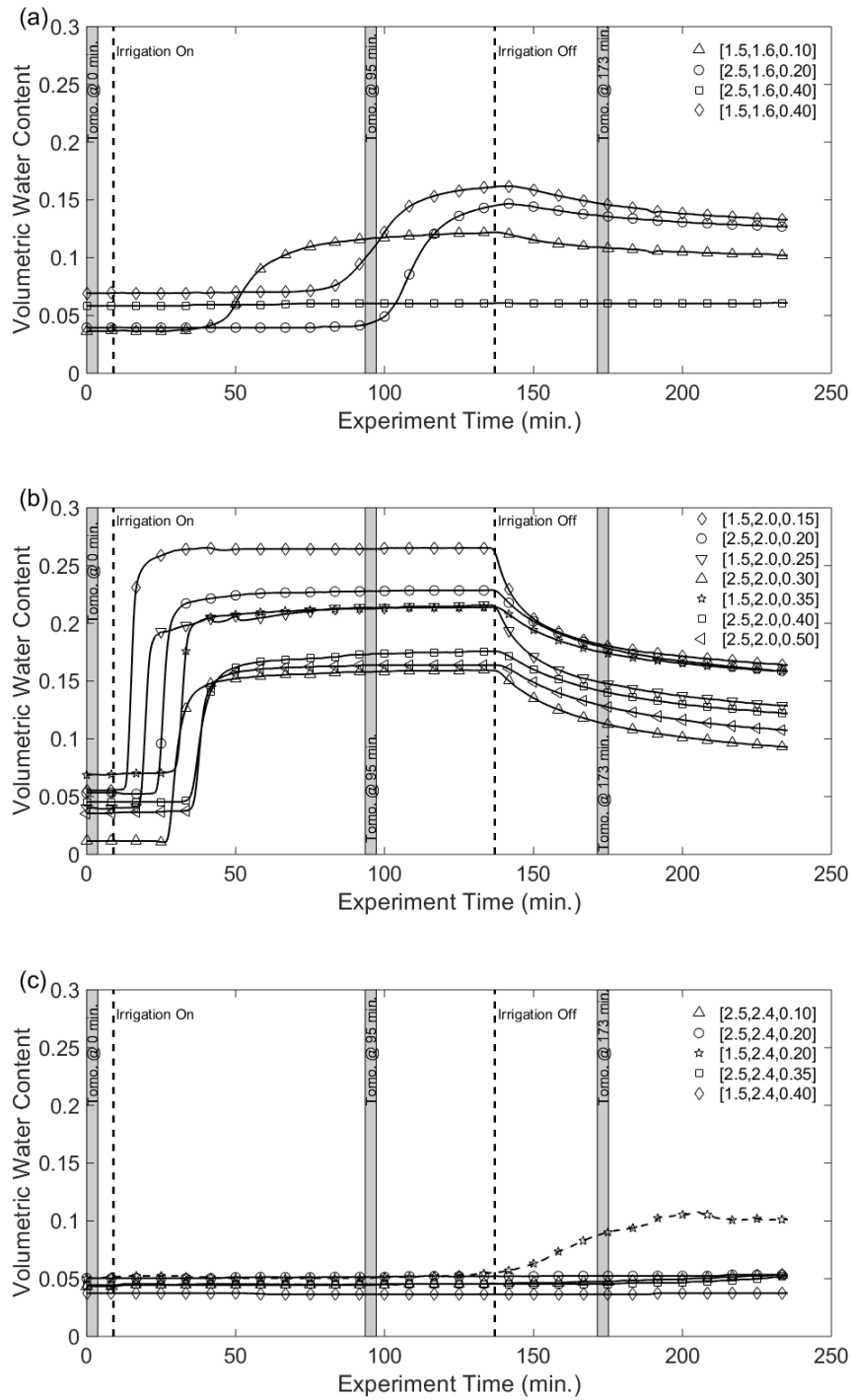
435



437

438 Figure 4: Panels (a, f, and k) are common-offset GPR data collected during the experiment. Panels (b-d, g-i, and l-n) are CMP data collected during the experiment.
 439 Arrivals annotated are the sand layer reflection (B) and wetting front reflection (W). Panels (e, j, and o) show tomography results for the corresponding GPR data.
 440 Vertical lines indicate the lateral extent of the wetted surface. Shapes correspond to the soil moisture data for the given y-location in Figure 5, colors correspond to
 441 the measured soil moisture. Adjacent symbols are from probes that are located at different x-locations, but identical depths.

442 **Figure 5**



443
 444 Figure 5: Soil moisture probe data from the in-situ moisture probes along the GPR line at a) y = 1.6 m; b) y = 2.0 m;
 445 and c) y = 2.4 m. Vertical dashed lines indicate the start and stop of irrigation. Gray bars indicate the times when data
 446 in Figure 4 were collected. Symbols for a given data set match those on Figures 4e, j, and o. Soil moisture data were
 447 collected 60 minutes beyond the end of GPR data collection.